Rev. Roum. Sci. Techn.– Électrotechn. et Énerg.
Vol. **71**, *1*, pp. 151–156, Bucarest, 2026

EVALUATION FOR THERMAL ANALYSIS OF DC MOTORS IN ELECTRIC VEHICLES

SURESH PANDIARAJAN PERUMALSAMY[1], VANAJA NARAYANASAMY[2], KRISHNA PRAKASH ARUNACHALAM[3], PRASANTH BALASUBRAMANIAN[4]

Keywords: Cooling; DC series motor; Temperature; Thermal analysis.

Series-wound DC motors remain attractive in many applications due to their simplicity, robustness, and cost-effectiveness. However, their performance and service life depend heavily on effective thermal management. This study presents a detailed investigation into the modeling, simulation, experimental validation, and thermal analysis of a series-wound DC motor under various cooling strategies. A thermal circuit model was developed in LabVIEW to predict temperature rise in different motor components, while a custom experimental setup was constructed to directly measure torque, current, and temperature during real-world operation. Multiple thermocouples were embedded in the motor to capture temperature distributions with high accuracy, and LabVIEW was employed for precise data acquisition and processing. Experimental results were used to refine and assess the thermal model, enabling a comparison between solid and optimized motor configurations. The findings highlight the impact of selecting appropriate cooling techniques on reducing hot-spot temperatures, thereby improving overall motor efficiency, reliability, and lifespan.

1. INTRODUCTION

In today's world, electric motors play a critical role in driving mechanical development, as they enable the conversion of electrical energy into mechanical energy. Broadly, motors are classified into two types: AC motors, which operate on alternating current, and DC motors, which rely on direct current. DC motors are further divided into four categories: permanent magnet motors, series-wound motors, shunt-wound motors, and compound motors. While their construction may vary, most DC motors share a similar internal operating principle, which is based on Fleming's left-hand rule [1].

The "series motor," also known as the series-wound DC motor, connects its armature and field windings in series. Because the field strength varies directly with armature current, these motors deliver exceptionally high starting torque, making them suitable for applications with high inertia at startup. However, their speed is highly load-dependent, ranging widely between no-load and heavy-load conditions, which limits their use in applications requiring constant speed [2]. Series motors are also sometimes called universal motors, as they can operate on both AC and DC supplies. Their simple, robust design, strong torque, and ease of maintenance continue to make them relevant despite the growing use of brushless DC and AC induction machines [3].

Series-wound DC motors are commonly found in practical transportation and industrial systems. For example, electric rickshaws and three-wheelers rely on these motors to provide high torque at low speeds, essential for transporting passengers and goods in both urban and rural areas [4]. In rural settings, they are also used in small-scale agricultural machinery such as irrigation pumps, threshers, and chaff cutters, where durability and torque are more important than cutting-edge technology. Series motors are employed in electric traction systems for trains, trams, and electric vehicles (EVs), as well as in cranes, hoists, and winches, where heavy lifting requires strong starting torque. They also find use in mining equipment, conveyors, and windlasses, where their high torque characteristics are particularly advantageous.

DC motors, often called brushed motors, are still utilized in certain electric vehicle applications. They require brushes and a commutator to switch the current direction within the windings. Their high starting torque and relatively simple design make them suitable for vehicles requiring frequent acceleration and deceleration. While AC machines dominate the mainstream EV market, DC motors continue to power smaller electric vehicles such as e-bikes and scooters due to their lower cost and ease of control [5]. The development of specialized electric motors for vehicle applications is a collaborative effort between manufacturers, research institutes, and universities. Today, several motor technologies—including DC motors, induction motors, and variable reluctance motors—are applied in automotive powertrains, with three-phase induction and series DC motors among the most widely used [6].

The rapid adoption of electric and hybrid electric vehicles (EVs and HEVs) highlights the importance of understanding and optimizing electric powertrains [7]. Research into motor design and operation has expanded significantly, reflecting the critical role of electrical machines in sustainable mobility [8]. With increasing concerns about fossil fuel depletion, pollution, and climate change, EVs are recognized as central to global clean-energy strategies. In many regions, the transition toward EV adoption has shifted from being primarily policy-driven to increasingly market-driven [9,10]. Within EVs, electrical machines account for a significant share of performance and efficiency, underlining their importance to both industry and academia.

Electric motors and drive systems represent nearly 64% of industrial electricity consumption. Energy losses within these systems—arising from eddy currents, winding resistance, armature, and field losses—manifest as heat, raising component temperatures and reducing efficiency. These thermal effects influence both torque and rotational speed. If temperature rise is not properly managed, motor lifespan can be significantly reduced [11]. Effective cooling strategies are therefore essential to dissipate excess heat and protect motor integrity [12].

Several advanced approaches have been studied to

---

[1] P.S.R.R College of Engineering, Sivakasi, Tamil Nadu, India. Email: sureshpandiarajan81@gmail.com
[2] Mepco Schlenk Engineering College, Sivakasi, Tamil Nadu, India. E-mail: nvanaja@mepcoeng.ac.in
[3] Departamento de Ciencias de la Construcción, Facultad de Ciencias de la Construcción Ordenamiento Territorial, Universidad Tecnológica Metropolitana, Santiago, Chile. E-mail: k.prakash@utem.cl
[4] Anna University, Chennai, Tamil Nadu, India. Email: prasantheeeau@gmail.com

DOI: 10.59277/RRST-EE.2026.1.25

enhance motor performance. For example, a generalized 13-level symmetrical inverter topology has been proposed to improve power quality [13]. This design, based on six DC sources and twelve semiconductor switches, can be cascaded to increase the number of levels, though at the expense of higher cost and complexity. Using nearest-level modulation for gate signal generation, the topology was benchmarked against existing designs, with key performance parameters including total harmonic distortion (THD), cost per level (CCPL), total standing voltage (TSV), and efficiency (η).

Other studies, such as those using Particle Swarm Optimization (PSO), have focused on parameter estimation for permanent magnet synchronous motors (PMSMs). PSO has been applied to estimate online parameters using real-time current and speed measurements, and its accuracy and stability have been validated through laboratory experiments at Ecole Centrale de Nantes. A comparative analysis demonstrated PSO's effectiveness over other algorithms for identifying PMSM parameters [14].

Raja et al. (2023) present a case-specific thermal analysis of a permanent magnet motor in EVs, simulating heat losses and temperature distribution over driving cycles to highlight risks such as demagnetization and insulation failure, while stressing the importance of cooling design [15]. In contrast, Lourembam et al. (2025) provide a state-of-the-art review of electric motor modeling and design for e-mobility, covering electromagnetic, thermal, and mechanical aspects, and identifying gaps in cooling strategies, multiphysics integration, and optimization [16]. Together, these studies show the field's dual needs: detailed experimental validation under realistic conditions and broader multiphysics frameworks for design, both of which your work addresses by combining comparative cooling analysis with validated modeling.

Building on these foundations, this paper focuses on improving the thermal management of series-wound DC motors. Specifically, it investigates power losses, heat flow, and cooling methods applied to the motor's core, housing, and windings. Both experimental testing and thermal modeling are carried out to analyze heat flux relative to temperature distribution under various cooling designs. The goal is to develop cost-effective cooling solutions that improve motor efficiency and extend operational life. Special emphasis is placed on oil-cooling mechanisms and their effect on heat distribution across motor components. By ensuring optimal temperature limits, the study aims to minimize thermal degradation and enhance performance under diverse operating conditions.

A key strength of this work lies in the experimental validation performed in real-world urban environments, producing reliable and application-oriented results. Compared with conventional laboratory testing, this approach provides faster, more cost-effective insights into thermal performance. Based on these findings, the study proposes practical guidelines for optimizing the design and operation of series-wound DC motors, including the selection of appropriate coupling configurations and oil-cooling strategies tailored to specific applications.

2. **THERMAL ANALYSIS OF DC SERIES MOTOR**

2.1. DC SERIES MOTOR – INTRODUCTION AND SIMULATION

Like shunt-wound and compound-wound DC machines, a series DC motor is a self-excited type of motor that operates using its own supply. Its name comes from the internal series connection between the armature winding and the field winding, as shown in Figures 1 and 2. Because a single voltage source energizes both the field winding and the armature, the motor is classified as self-excited. Compared to a shunt motor, a series motor delivers much higher starting torque. This is because, at startup, the same current flows through both the armature and the field winding. The resulting increase in magnetic flux produces a strong electromagnetic force, giving the motor significantly greater starting torque. Table 1 summarizes the traction motor's key ratings, geometry, and limits used in modeling/experiments.

Table 1

Key specifications.

Parameter	Value
Rated mechanical power	100 kW
Rated speed (nominal test point)	1000 rpm
Rated torque	955 N·m
Rated voltage	220 V
Rated current	511 A
Electrical limits used in study	I ≤ 511 A; V ≤ 220 V
Geometric envelope (L×W×H)*	440 × 1090 × 1155 mm

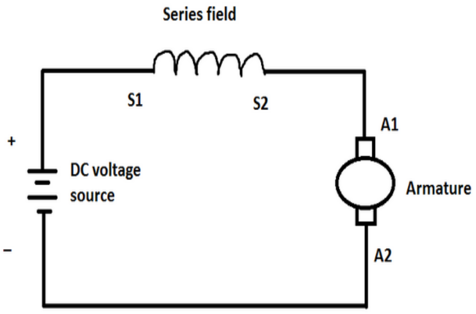

Fig. 1 – Series connection of DC motor.

Using a block diagram and the equations from (1) to (6), a series DC motor can be depicted. The following equations, which were represented as block diagrams, are obtained through performing the Laplace transform of these equations and assuming that the initial conditions are zero. Electrical and mechanical parts can be used to replicate the characteristics of series DC motors. DC motor simulation has been carried out in MATLAB environment using Simulink library/Simscape as shown in Figure 2.

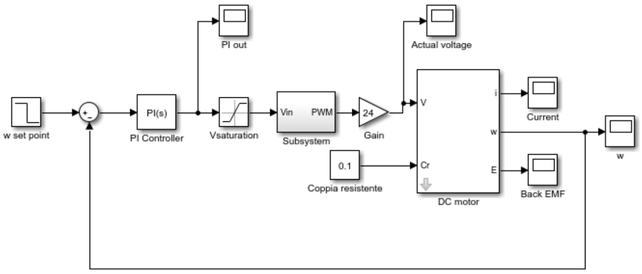

Fig. 2 – Simulation of a DC series motor.

Two scopes were used during the simulation, and they generated output values for armature current and electromagnetic torque.

$$V = R_a i_a + R_f i_f + sL_a i_a + sL_f i_a + \omega_r L_{af} i_a, \tag{1}$$

$$i_a = i_f, \tag{2}$$

$$i_a = \frac{1}{(R_a+R_f+sL_a+sL_f)}\left(V - \omega_r L_{af} i_a\right), \tag{3}$$

$$T_e = (sJ + B_m)\,\omega_r + T_l, \tag{4}$$

$$T_e = L_{af} i_a^2, \tag{5}$$

$$\omega_r = \frac{1}{(sJ+B_m)}\left(L_{af} i_a^2 - T_l\right), \tag{6}$$

The simulation of the DC series motor was performed in the MATLAB environment. From the simulation results, the armature current and the corresponding electromagnetic torque were recorded using scope outputs. These values were then used to plot the characteristic relationship between armature current and torque, as illustrated in Figure 3.

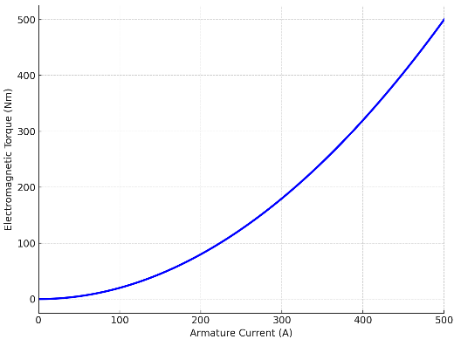

Fig. 3 – Torque current characteristics of DC series motor.

Electric motors function as energy converters, transforming electrical input into mechanical output. However, this process is not entirely efficient, as certain losses occur and manifest as heat within the machine. The two dominant sources of this heating are ohmic (resistive) losses and mechanical friction losses (resistive, or Joule, heating). The ohmic loss, also known as Joule heating, depends on the winding resistance (R_e) and the instantaneous motor current (I), and can be expressed as:

$$P_e = I^2 R_e. \tag{7}$$

At light motor loads, mechanical friction constitutes the primary source of energy loss, while at higher loads, ohmic (resistive) losses become the dominant contributor.

3. EXPERIMENTAL SETUP

As part of the laboratory setup, a mechatronic system was integrated into a test vehicle to enable real-time evaluation of traction motors, transmissions, and lithium-ion battery packs designed for both hybrid (blended) and fully electric automobiles. The system is composed of two primary mechatronic modules: electronic and electro-mechanical.

The electro-mechanical module serves as the core of the framework and includes traction motors, traction batteries, and mechanical subsystems. To reduce cost and simplify stress analysis during the design stage, the mechanical components were selected from commonly available locomotive parts. These include the differential, wheels, gearbox, belt or chain drive, and clutch. Together with the traction motor and battery, each of these elements can function independently or as part of different robotic/mechatronic configurations within the testing system.

The dimensions and arrangement of all components were designed to ensure that the system could be installed in a test vehicle capable of performing experimental trials under real-world operating conditions. In this setup, the electromechanical module is coupled to the rear running gear of the test vehicle. Figures 4 and 5 illustrate the layout and block diagram of the electrically powered module, respectively. Figure 4 also shows the airflow and heat transfer generated by an axial fan–driven forced-air cooling system attached to the electric motor. The components in Figure 6 are identified as follows: (1) battery, (2) electronic control system, (3) traction motor, (4) differential with gearbox and wheels, (5) belt drive, and (6) gearbox. Finally, Figure 6 presents the thermal flow paths corresponding to the three different cooling configurations analyzed in this study.

Fig. 4 – Picture of electromechanical module in real time condition.

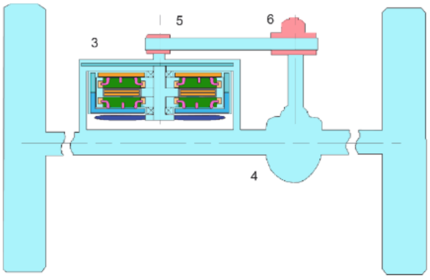

Fig. 5 – Block-diagram of module.

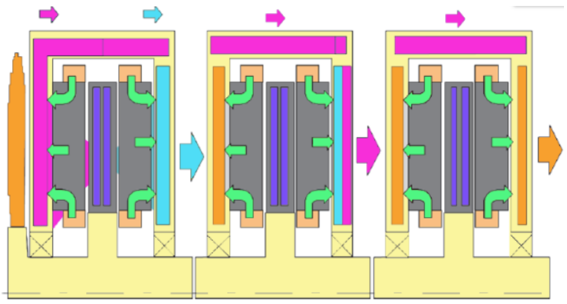

Fig. 6 – Thermal paths for three distinct types of cooling systems: (a) forced air cooling via fan-equipped electric motors; (b) one-sided liquid cooling electric motors; and (c) double-sided liquid cooling electric motors.

The BPM-Therm software package was employed to develop a simplified thermal model of the DC series motor. The motor under study was characterized by the following rated electromagnetic parameters: speed of 1000 rpm, torque of 955 Nm, power output of 100 kW, voltage of 220 V, and current of 511 A. The geometric dimensions used in the analysis were 440 × 1090 × 1155 mm.

In this framework, BPM-Therm incorporates inputs from multiple motor features, including axial forces, cooling fins, housing covers, insulation layers, and other structural elements, to model the thermal transfer pathways. Microsoft Excel was used to calculate the required input parameters and to serve as an interface for automatically importing the data into the simulation, both prior to and after processing. The central aim of the model is to predict conductive heat transfer through the laminated silicon steel core, the motor's end flanges, and its ribbed, radiator-like housing, which is securely fastened to the stator assembly. Heat dissipation is achieved through different cooling methods—either airflow or liquid circulation—via ventilation ducts or cooling jackets integrated into the housing.

To validate the model, thermocouples were installed within the motor assemblies to monitor operating temperatures under real conditions. At the nominal motor speed of approximately 1000 rpm, thermocouple readings were continuously recorded with an accuracy of about ±0.5 °C. Experimental temperature-time data were approximated using curve-fitting functions implemented in LabVIEW. The recorded temperature profile $T_{exp} = F(t)$ was fitted with empirical coefficients a_k, b_k, and c_k chosen to ensure close agreement between the experimental data and the predicted output of BPM-Therm. During calibration, this relationship is represented by a nonlinear equation of the form:

$$T_{exp} = a_k \exp\{b_k[\exp(c_k t)]\}. \tag{8}$$

As a result of calibration, the parameter values were determined as $a_k = 85$, $b_k = -0.652$, and $c_k = -0.08$. When the cooling process reaches equilibrium—*i.e.*, when the nonlinear Equation (8) converges over time—the measured temperature of the system under investigation remains constant.

$$T_{exp}\left[\varphi_l(t^{(1)})\right] - A_{exp}\left[\varphi_1(t^{(2)})\right] = 0. \tag{9}$$

The maximum value of T_{exp}, obtained from the experimental testing procedures, is identified and defined as $T_{exp} = T_e$, which serves as the reference point for the system's equilibrium temperature. Likewise, Equation (9) determines the maximum value of T_{calc} at the point where the numerical results stabilize. This provides an approximation of the graphical representation of the estimated thermal response for the tested installation.

An automated comparison is then performed between the experimental (T_{exp}) and calculated (T_{calc}) temperature curves. If the difference between these two exceeds 3–4 %, certain input parameters in the BPM-Therm thermal model must be corrected. Once the error margin is within the acceptable 3–4% range, the model is considered calibrated. For each assembly tested, trials are conducted to determine the time at which equilibrium temperature T_e is reached, ensuring consistency between the simulation and experimental data.

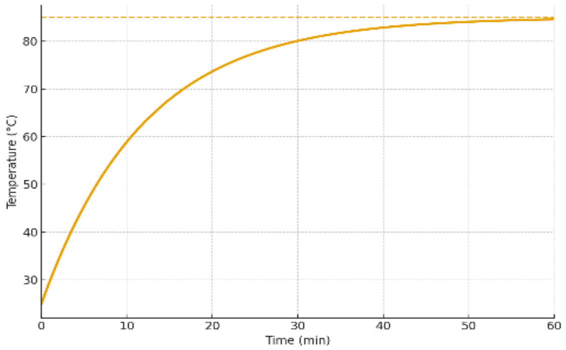

Fig. 7 – Heat *versus* period found during an individual installation of an air-cooled motor is represented graphically in LabVIEW as $T = F(t)$.

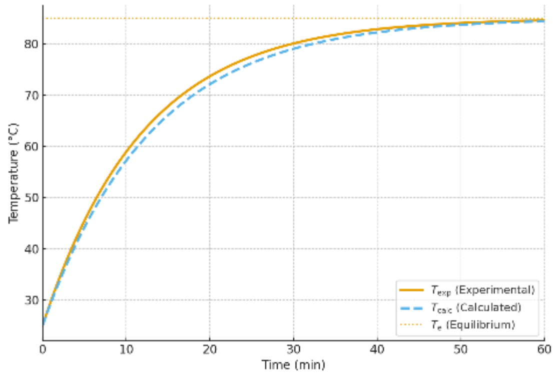

Fig. 8 – Comparative examination and assessment of $T_{calc} = T_e$.

The calibration procedure for the ventilated motor setup is illustrated in Fig. 7 and 8. In this configuration, a fan is employed to cool the left flange, while forced ventilation is applied to dissipate heat from the field windings. To determine the temperature–time dependencies, the thermal model imports the necessary components and parameter values directly from the BPM-Therm database.

Maintaining the thermal stability of a DC series motor during experimentation is essential, as it not only ensures the safety of the machine but also enhances the accuracy of the results. Thermocouples embedded within the assemblies enable continuous monitoring of the winding temperatures and other critical components. The installed cooling system guarantees unobstructed airflow, allowing effective dissipation of the heat generated during operation. Achieving proper temperature control requires a coordinated approach that combines continuous monitoring, efficient cooling, and regulated operation. By implementing these measures, the motor is kept within safe thermal limits, thereby ensuring more precise and reliable experimental outcomes.

3.1. EXPERIMENTAL RESEARCH

In the liquid cooling system, glycol (antifreeze) is used as the working fluid. The coolant enters the system at 20 °C and reaches a maximum of 80 °C once the equilibrium temperature (T_e) is achieved. The initial ambient temperature is also 20 °C. The test setup assumes an initial airflow of 138 m³/h and a constant coolant flow rate of approximately 8 L/min at a pressure of 1.5 bar. During the tests, no energy recuperation or internal combustion engine (ICE) assistance is employed.

3.2. THERMAL MODELING AND EXPERIMENTAL TEST CALIBRATION

The first stage of validation was performed under stationary operating conditions. For this purpose, the vehicle was mounted on a braking evaluation stand designed to apply sufficient braking torque to the rear wheels, limiting the motor current to below 40 A for a continuous 60-minute heavy-load test. These trials allowed the identification and correction of limitations within the thermal model. The deviation between simulated and experimentally measured temperatures remained within 3–4%. This calibration procedure was carried out for all selected assemblies of the motor, following the methodology outlined earlier and illustrated in Fig. 8 and 9.

3.3. EXPERIMENTS CONDUCTED IN A REAL SETTING

After calibration, field experiments were performed on a road segment containing a short overpass with a slope of up to 4 %. Under dry-weather conditions, the test vehicle achieved an average speed of 40 km/h over a 60-minute trial period. Each test began with the traction motor operating steadily at approximately 1000 rpm and the traction battery pack fully charged. Prior to every run, all key parameters—including ambient temperature, coolant temperature, motor load, and vehicle speed—were verified against the intended test configuration. Each trial was repeated three times under identical conditions, and deviations from the expected results were corrected using standardized procedures.

3.4. THERMAL ANALYSIS AND RESEARCH OUTCOMES

The calibration curve of temperature versus time, generated in LabVIEW, is presented in Figure 9, showing $Texp = F(t)$ at the motor's left flange. Following calibration, the experimental and predicted datasets were aligned in Microsoft Excel using the approximations described in Equations (8) and (9). The resulting comparison of $T_{exp} = F(t)$ and $T_{calc} = F(t)$ is presented in Figure 10. To ensure that the calculated equilibrium temperature ($T_{calc} = T_e$) remained within the acceptable 3–4% deviation, the airflow parameter in the BPM-Therm module was adjusted from its initial value of Q=138 m^3/h to Q=240 m^3/h.

Figure 9 illustrates the comparison between predicted and experimental temperature rise in the assembly located behind the motor's left flange under forced-air cooling. This assembly was initially calibrated following the previously described procedure. However, even during the first field tests, a significant discrepancy was observed between the measured and predicted temperatures at the motor's right side.

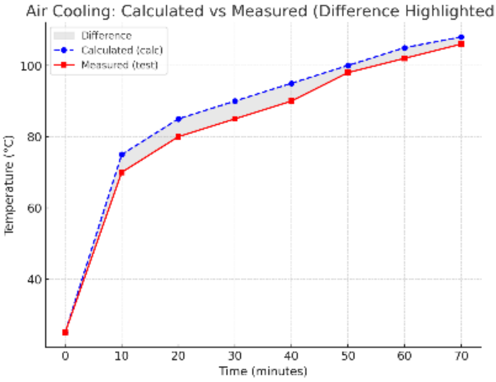

Fig. 9 – Assembly thermal measurement test on left edges with ventilation.

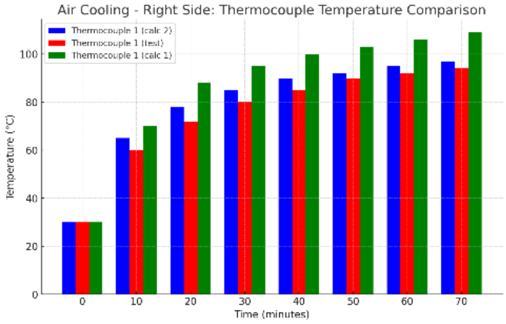

Fig. 10 – Test for assembly temperature calibration on the appropriate flanges when using air cooling.

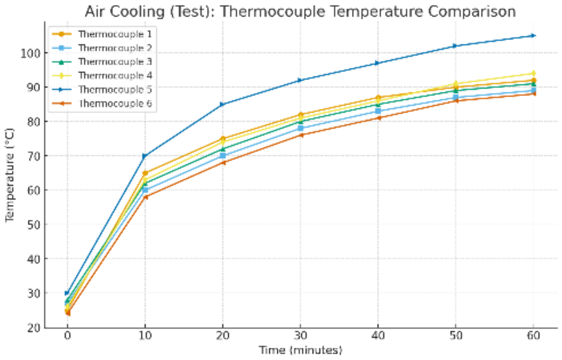

Fig. 11 – Experimental heat results graph for air-cooled motor.

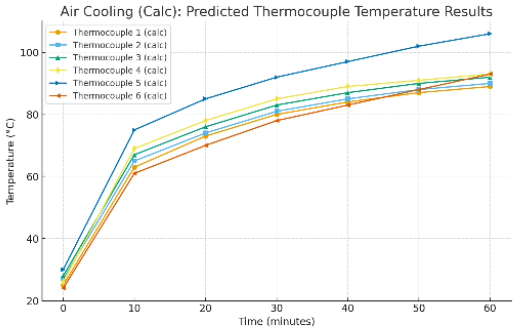

Fig. 12 – Predicted temperature results graph for air-cooled motor.

The temperatures recorded under real operating conditions were consistently lower than those observed during calibration of the same component. This discrepancy suggests that, in actual environments, forced airflow around the housing's right end promotes additional convection that was not accounted for during the initial calibration. To properly replicate conductive heat transfer in the thermal model, all other component parameters must remain unchanged. Therefore, the effect of convection at the right-flange installation must be incorporated into the calibration process to achieve accurate predictions. The results of this secondary calibration for the motor's right stationary section are presented in Figure 10, demonstrating close agreement with the experimental data collected under real conditions. Figures 11 and 12 show the measured and predicted heat profiles for the air-cooled motor.

The measurement and simulation graphs reveal that the deviation between experimental and predicted temperatures remains within 3–4 % for both single-sided and double-sided water cooling, which is an acceptable margin. This correspondence is illustrated in Figure 11, where direct comparisons between experimental and simulated equilibrium temperatures are used to evaluate model accuracy across cooling methods, rather than relying on multiple overlaid graphs. The summarized values for each motor assembly, including the equilibrium conditions of both experimental and predicted results, are presented in the accompanying table.

Some variation was observed between the equilibrium temperatures measured during one-sided liquid cooling in field tests and those obtained during stationary calibration. This difference is most likely attributable to additional convection effects caused by on-road airflow, since the motor is mounted within the sub-sprung mass of the test vehicle. By contrast, the deviations observed under one-sided air cooling were small and within permissible limits, requiring no further adjustment of the thermal model. For two-sided liquid cooling, the experimental and predicted results were nearly identical, confirming the reliability of the model under those conditions. The validation of the BPM-Therm simulation with experimental results is provided in Table 2.

Table 2

Validation of BPM-Therm simulation with experimental results

Cooling layout	Exp–Sim agreement	Notes
Forced-air	Within 3–4 % after airflow correction	Airflow adjusted from 138 → 240 m³/h to match field conditions
One-sided liquid	Within 3–4%	Slight on-road deviation due to extra convection
Two-sided liquid	Nearly identical (≤ 3–4%)	Best match; confirms model reliability
Overall	Typical error 3–4 %; max < 7%	Across all configurations

The controller plays a critical role in influencing the motor's thermal behavior because it directly governs current magnitude, duty cycle, and switching patterns. Under high torque demand, the controller supplies higher armature current (up to the rated 511 A), which proportionally increases copper losses (I^2R) and contributes to rapid temperature rise. Similarly, voltage modulation and commutation introduce iron and switching losses that add to the total heat load. During experimental runs, current limiting and pulse-width modulation (PWM) strategies implemented in the controller were essential in constraining excessive heating, ensuring the motor operated within safe thermal margins. Thus, the observed temperature profiles are not only a function of the cooling method but also of the controller's operating logic, which balances performance and thermal safety.

Future work will cast the design as a multi-objective optimization over thermal and dynamic performance. Specifically, we will seek Pareto-optimal trade-offs among (i) peak winding/flange temperature T_{peak}, (ii) thermal settling time to 95 % of equilibrium τ_{95}, (iii) copper loss $P_{\mathrm{Cu}} = I^2R$, and (iv) coolant/fan power P_{aux}, subject to $T \le T_{limit}$, *required torque delivery $\tau \ge \tau_{req}$, and electrical/mechanical limits ($I \le 511$ A, $V \le 220$ V) and packaging constraints of the cooling jacket. Decision variables will include coolant flow Q, fan speed ω_{fan}, jacket channel dimensions, and drive controller gains (K_p,K_i). Solutions will be reported as Pareto sets (*e.g.*, via NSGA-II) to quantify the thermal–efficiency trade-space for the calibrated motor model.

5. CONCLUSION

In this study, a comprehensive thermal analysis of a 100 kW series-wound DC motor for EV applications was carried out through both experiments and simulations under forced-air, one-sided liquid, and two-sided liquid cooling. The results showed that the calibrated BPM-Therm model accurately predicted motor temperature rise, with deviations from experiments remaining within 3–4 % and never exceeding 7 %. This validation demonstrates that the proposed framework is reliable for predicting motor thermal behavior under varied cooling strategies. The novelty of this work lies in the systematic comparison of multiple cooling layouts on the same traction motor, combined with a validated modeling approach that incorporates airflow correction and curve-fitting of transient temperature profiles. By providing a clear methodology and benchmark data, the study not only enhances understanding of thermal performance in traction motors but also offers a practical tool for researchers and designers to optimize cooling configurations, reduce development time, and improve the safety and reliability of electric vehicle powertrains.

CREDIT AUTHORSHIP CONTRIBUTION

Suresh Pandiarajan Perumalsamy: presented idea
Vanaja Narayanasamy: theory and computations
Krishna Prakash Arunachalam: simulations and results
Prasanth Balasubramanian: results analysis

Received on 30 January 2025

REFERENCES

1. K. Shrivastava, M. Pawar, *A review on types of DC motors and the necessity of a starter for their speed regulation*, International Journal of Advanced Research in Computer and Communication Engineering, **5**, *4*, pp. 61–63, (2016).
2. Q. Duan, Y. Zhang, *Analysis and implementation of series excitation DC motor control system*, Joint International Information Technology and Artificial Intelligence Conference (ITAIC), Chongqing, China, (2020).
3. J.U. Liceaga-Castro, I.I. Siller-Alcalá, J. Jaimes-Ponce, R.A. Alcántara-Ramírez, E.A. Zamudio, *Identification and real-time speed control of a series DC motor*, Mathematical Problems in Engineering, (2017).
4. G. Ramani, K.K. Kumar, M. Chitra, M.P. Selvam, N. Selvam, S. Sudha, *Performance improvement of lithium-ion battery for battery EVs*, International Conference on Communication, Computing and Internet of Things (IC3IoT), Chennai, India, (2024).
5. M. Matteo, A. Marcus, D. Arent, M. Bazilian, P. Cazzola, E. Dede, J. Farrell, C. Gearhart, D. Greene, A. Jenn, *The rise of electric vehicles—2020 status and future expectations*, Progress in Energy, **3**, (2021).
6. K. Singh, H. Bansal, D. Singh, *A comprehensive review on hybrid electric vehicles: architectures and components*, Journal of Modern Transportation, **27**, pp. 77–107, (2019).
7. S. A, K. J, M. T, S. G.Á., *Dynamic test measurements and simulation on a series wound DC motor*, Applied Sciences, **11**, *4542*, (2021).
8. Gy. Szántó, G. Szíki, *Review of modern vehicle powertrains and their modelling and simulation in MATLAB/Simulink*, International Journal of Engineering Management and Sciences, **5**, pp. 232–250, (2020).
9. S. Chakraborty, N. Kumar, A. Jayakumar, S. Dash, D. Elangovan, *Selected aspects of sustainable mobility reveal implementable approaches and conceivable actions*, Sustainability, **13**, (2021).
10. A. Krings, C. Monissen, *Review and trends in electric traction motors for battery electric and hybrid vehicles*, in 2020 International Conference on Electrical Machines (ICEM), Gothenburg, Sweden, (2020).
11. A. Rambetius, *Thermal model for online temperature estimation of DC-link capacitor and DC-busbars considering variable switching frequency, variable modulation method, and variable coolant flow rate*, Transportation Electrification Conference & Expo (ITEC), Anaheim, CA, USA, (2022).
12. K. Zhou, *Computationally-efficient finite-element-based thermal and electromagnetic models of electric machines*, Ph.D. dissertation, University of Michigan, (2015).
13. R. Duirasamy, V. Thiyagarajan, *A novel fault-tolerant generalized symmetrical topology for renewable energy and electric vehicle applications*, Rev. Roum. Sci. Techn. – Électrotechn. et Énerg., **69**, *4*, pp. 383–388, (2024).
14. M. Abd El-Wanis, R. El-Sehiemy, M.A. Hamida, *Parameter estimation of permanent magnet synchronous machines using particle swarm optimization algorithm*, Rev. Roum. Sci. Techn. – Électrotechn. et Énerg., **67**, *4*, pp. 377–382, (2022).
15. S. Raja, S. Nandagopal, S. Muthiya, R, *Thermal analysis of an electric motor in an electric vehicle*, SAE Technical Paper 2023-01-0532, (2023).
16. L.R. Devi, S. Sreekumar, R. Bhakar, G. Dileep, S. Padmanaban, *Electric motor modeling, analysis, and design for E-mobility applications: a state of the art*, e-Prime – Advances in Electrical Engineering, Electronics and Energy, **12**, p. 100985, (2025).